Trans Indian Inst Met
https://doi.org/10.1007/s12666-022-02797-x

ORIGINAL ARTICLE

Experimental Investigation of Wire Arc Additively Manufactured Inconel 625 Superalloy

Uğur Gürol[1,2] · Mustafa Tümer[3] · Savas Dilibal[4]

Received: 6 July 2022 / Accepted: 7 October 2022

Abstract The aim of the present study was to reveal how the microstructure and mechanical properties of Inconel 625 superalloy produced via wire arc additive manufacturing (WAAM) changed in relation to deposition direction. Results showed that the microstructure mainly consists of columnar dendrites including some intermetallic and carbides constituents, which are Laves and NbC phases. The hardness values showed heterogeneous distribution from bottom to top and mainly change between 275 ± 15 to 298 ± 16 HV_5 except for the initial area reaching 318 ± 14 HV_5. The tensile test results revealed that the stress–strain responses of the samples change depending on the extracted direction. The lowest elongation was obtained at the transverse top and bottom regions with $33.5 \pm 1.5\%$ and $35 \pm 6\%$ while the highest elongation was obtained at the angular top and bottom with $48.5 \pm 6.7\%$ and $55.5 \pm 2\%$. The results confirmed the more pronounced difference with sample direction, indicating anisotropy in ductility.

Keywords Direct metal deposition · Wire arc additive manufacturing · Inconel 625 · Intermetallic

✉ Uğur Gürol
ugur.gurol@yahoo.com

1 Metallurgical and Materials Engineering Department, Engineering Faculty, Istanbul Gedik University, Istanbul, Turkey

2 Research & Development Center, Gedik Welding Inc., Istanbul, Turkey

3 Welding Technology Program, Kocaeli University, Kocaeli, Turkey

4 Mechatronics Engineering Department, Engineering Faculty, Istanbul Gedik University, Istanbul, Turkey

1 Introduction

Wire arc additive manufacturing (WAAM) is one of the emerging direct metal deposition technologies to manufacture large-scale components through the layer-by-layer process [1]. The weldability of the metals provides a significant function for fabricating WAAM-based components via employing various commercially available welding wires. Many metallic components such as aluminum-based, nickel-based, and titanium-based alloys and steels can be produced using the robotic WAAM systems [2–5]. A small batch with large-scale metallic components can be manufactured through the WAAM technologies in many fields of the industry.

The Inconel 625 superalloys are widely used in underwater, aircraft, and chemical applications within the temperature range starting from cryogenic conditions to the elevated high temperatures due to the high corrosion and oxidation resistance in aggressive environments [6]. The Inconel 625 is in the austenitic face-centered-cubic (FCC) structure with secondary phases which are NbC [7–9] and Laves phase. These Ni-based superalloys with nickel–chromium matrix are strengthened through solid solution hardening [10] of Nb and Mo refractory metals [11]. Many different carbide forms can precipitate depending on the aging time and applied temperature. The distribution and size of the Laves phase are determined by examining the form of the columnar structure that occurs after solidification. The secondary phases which are formed during solidification are the light-colored phase with an amorphous or eutectic morphology along the dendrites during the solidification of the matrix.

Metal additive manufacturing can be classified based on the applied power source, the feeding material, and the size of the product. Depending on the source of the energy, the direct energy deposition (DED) process can be categorized

Published online: 07 January 2023

into the laser beam [12], electron beam [13], and wire arc additive manufacturing technologies [14]. In the literature, many investigations have been made on the manufacturing and characterization of the Inconel 625 superalloy with its powders through the laser-based or electron beam-based direct energy deposition processes [15–18]. The effect of metal powder characteristics on the product quality is mainly studied in these experimental works. In the microstructural analysis, a columnar dendritic microstructure which can cause structural defects with decreased mechanical strength was examined on the DED-laser processed components [17].

Arc welding is applied with the welding wires as a DED-arc in the WAAM-based process. In the literature, it is experimentally revealed that the DED-processed samples show superior mechanical properties with higher yield strength and higher ultimate tensile strength than the wrought Inconel 625 and powder bed fusion-based counterparts [19]. Recently, Inconel 625 superalloy has been fabricated via the DED-arc process [20]. It has been reported that the dendrites grow perpendicular to the substrate. Additionally, the microstructure of the deposited layers depends on the cooling rate and the heat dissipation. A microstructural variation can be attributed to the cooling rate in the bottom, middle and top layers.

The aim of this work is to evaluate the deposited Ni-based metal which is produced for linear applications with moderate wall thickness in the laboratory and is exposed to several thermal cycles with the influence of microstructural changes and their effects on mechanical properties dependent on the applied test direction as well as the intermetallic phases formed during solidification. In this paper, the microstructure and hardness analyses are conducted for the WAAM-deposited Inconel 625 samples. Additionally, tensile test specimens with the longitudinal (x–z) and transverse (y–z) axis and with an angle of 45° to the longitudinal axis are extracted from the as-deposited Inconel 625 component. The tensile test responses of the WAAM-deposited Inconel 625 superalloy are examined using the uniaxial tensile test results. In summary, the present study provides critical insight into the microstructural characteristics and mechanical properties of the as-deposited Inconel 625 component for facilitating fundamental understanding of the WAAM-deposited samples.

2 Materials and Methods

The rolled 304 L stainless steel plate, with a size of 150 mm × 400 mm × 12 mm (width × length × height), was used as the substrate. To ensure repeatable and steady-state welding conditions, the substrates were polished and then cleaned with ethanol before welding. GeKa-Mac WB 500L GMAW machine with a water-cooled torch mounted on a 6-axis OTC Daihen FD-V8L was employed as the power source of the process as shown in Fig. 1. The ERNiCrMo3 wire with 1.2 mm diameter was used as the filler material with the chemical composition (wt%) and mechanical properties (yield stress, ultimate tensile strength, and elongation) given in Table 1. The WAAM process was carried out using the following parameters: an arc current of 160 A, an arc voltage of 22 V, a scan rate of 15 mm/s, and Argon + 2.5% O_2 as the shielding gas with the flow rate of 15 L/min. The parameters were decided with the considerations of bead geometry. The current and voltage values were set according

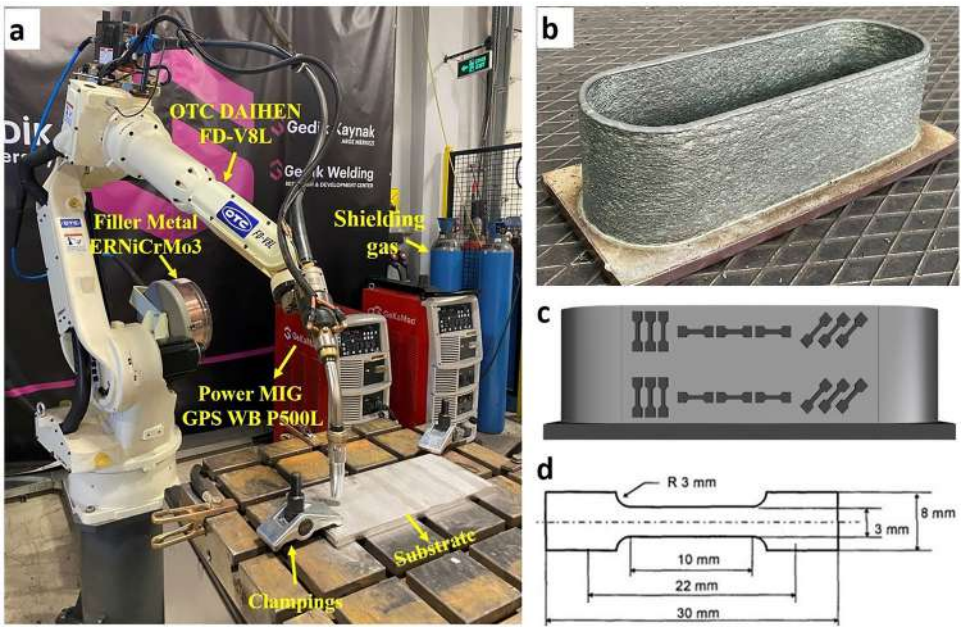

Fig. 1 a) The WAAM unit, b) the additively manufactured component, c) location of the extracted micro-tensile samples, d) dimensions of the micro-tensile samples

Table 1 Chemical composition (wt%) and mechanical properties of the filler metal

	C	Fe	Mn	Cr	Ni	Mo	Nb	Yield strength Rp0.2	Ultimate tensile strength Rm	Elongation (%)
ERNiCrMo3	0.02	1.0	0.20	22.0	62.25	9.10	3.50	540 MPa	800 MPa	38%

to the synergic program of the respective material. In this single-pass multi-layer deposition process, the GMAW torch was always stationary, and the work flat moved in the x-axis for the metal deposition. However, the layer thickness (offset value after each pass in z-axis) was 1.7 mm.

The continuous deposition results in heat build-up and slows down the cooling rate, especially in the later layers. Due to the heat build-up, the newly deposited molten metal and previously deposited layers tend to drip off and bulge, respectively, as reported by Ahsan et al. [4]. With the given conditions, the walled structure was fabricated, as seen in Fig. 1b. The final build dimensions were obtained using 60 welding passes as the thickness of 8 mm and height of 88 mm. No defects were observed from X-ray radiographs of the wall.

The cross-sectional surface was prepared using the standard grinding and polishing procedure, and electrolytically etched in 25% NaOH for 5 min to investigate microstructural phases that occurred during deposition. The macro- and microstructural evaluation was made using the Nikon SMZ745T stereo microscope and Leica DMi8 optical microscope, respectively. The horizontally (H), vertically (V) and angularly (A) oriented tensile test specimens were extracted using wire electrical discharge machining as shown in Fig. 1c, in order to investigate the mechanical properties and their anisotropy. Tensile tests were carried out on machined miniature plate specimens with a gauge section width, thickness, and length of 3.2 and 10 mm, respectively, as shown in Fig. 1d, using a WDM10 computerized electronic universal testing machine with a capacity of 10 kN. The dimensions of the miniature tensile specimens were designed according to ASTM STP 1329, and tests were performed at room temperature according to ASTM E8. Elongation values were determined using the total length of the miniature specimens, as gauge markings were masked by the discoloration of specimen surface during the test.

The micro-hardness tests were performed on specimens that were prepared for metallographic examination. The Vickers hardness distribution along the built direction starting from the substrate was measured by a DuraScan-70 G5 testing machine with a load of 5 kgf and a dwell time of 15 s applied for each indentation. Measurements were made at 0.5 mm distances from the substrate. The chemical compositions of GMAW-AM thin-walled components were analyzed using a thermo Scientific Spectrometer, as shown in Table 1. It is found that the percentage of the main elements of built thin-walled components fall in the value range of ERNiCrMo-3 wire given by the manufacturer.

3 Results and Discussion

In order to reveal the generated grain morphology, the LOM and SEM microstructures of the as-deposited component obtained by the MIG welding method were investigated in detail as shown in Figs. 2 and 3. Solid solution strengthened Ni-based alloys solidify as austenite, and its main microstructure is completely austenitic at the end of the solidification. However, the secondary phases are formed during the solidification as a result of the decomposition of alloying and stabilizing elements. The weld metal which was deposited with ERNiCrMo-3 filler wire formed a microstructure with a Ni-fcc matrix that solidified in columnar, cellular, and dendritic modes. The direction and form of the dendrites differ depending on the length of the sample, i.e., its thermal history. Complex cyclic thermal cycles during the WAAM process exhibit a higher temperature gradient resulting in epitaxial growth of columnar dendrites along the boundaries of the molten pool [4]. These differences indicate that the columnar growth from the bottom to top is supported via thicker columns and the dendritic structure is reduced as shown in Fig. 2. The columnar structure with lesser dendrite was quite dominant in the microstructure of the deposited weld metal top region. The grain direction and the size of the columns differed from the center to the edges as seen in Fig. 2b. Directional grains exhibit direction-dependent mechanical properties [21]. Figure 3 shows deposited weld metal microstructure taken from bottom beads. The higher cooling rate in the first layers of the WAAM process affected the texture and grain morphology. Significant dendritic growth was observed in columnar and cell-shaped dendrites [3]. Cellular, columnar and discontinuous dendrites were generated depending on solidification fronts. Besides, interface between beads occurred by subsequent passes changed microstructure from discontinuous dendrites to columnar microstructure.

Intermetallic phases bearing Mo and Nb during the solidification process occurred in tiny forms between dendrites and along with the columnar structure. The most common encountered secondary phases in nickel-based filler metal of the ERNiCrMo-3 type were NbC and Laves phases. Laves phase is an intermetallic compound with A_2B [22]

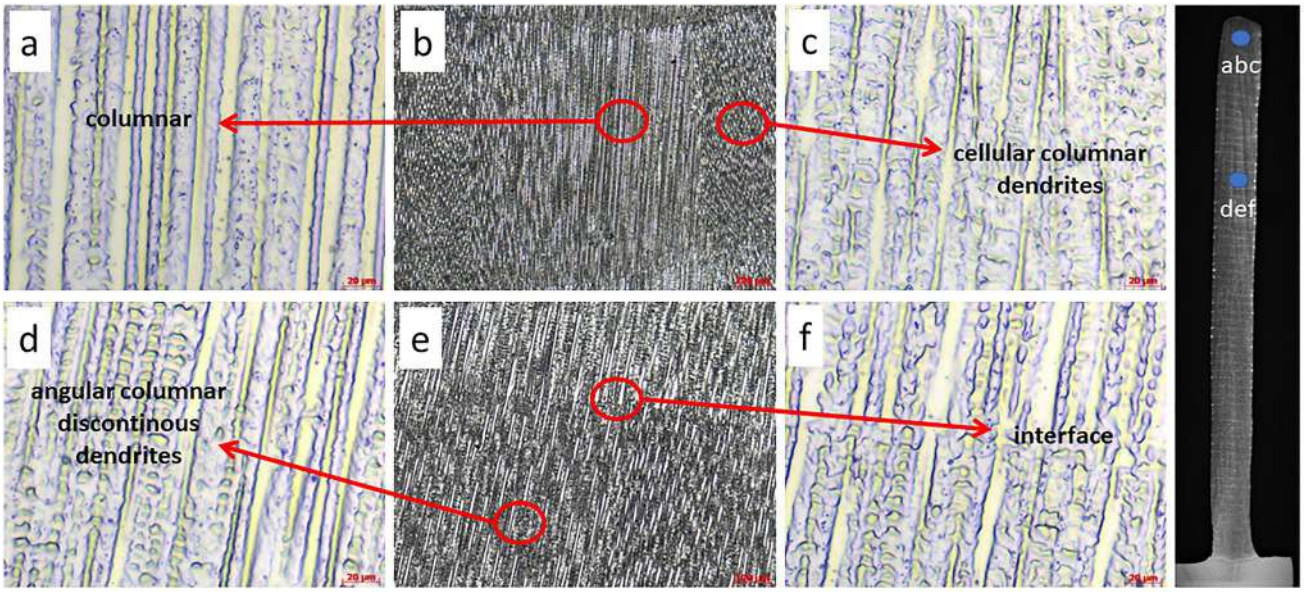

Fig. 2 Weld metal microstructure taken from top beads

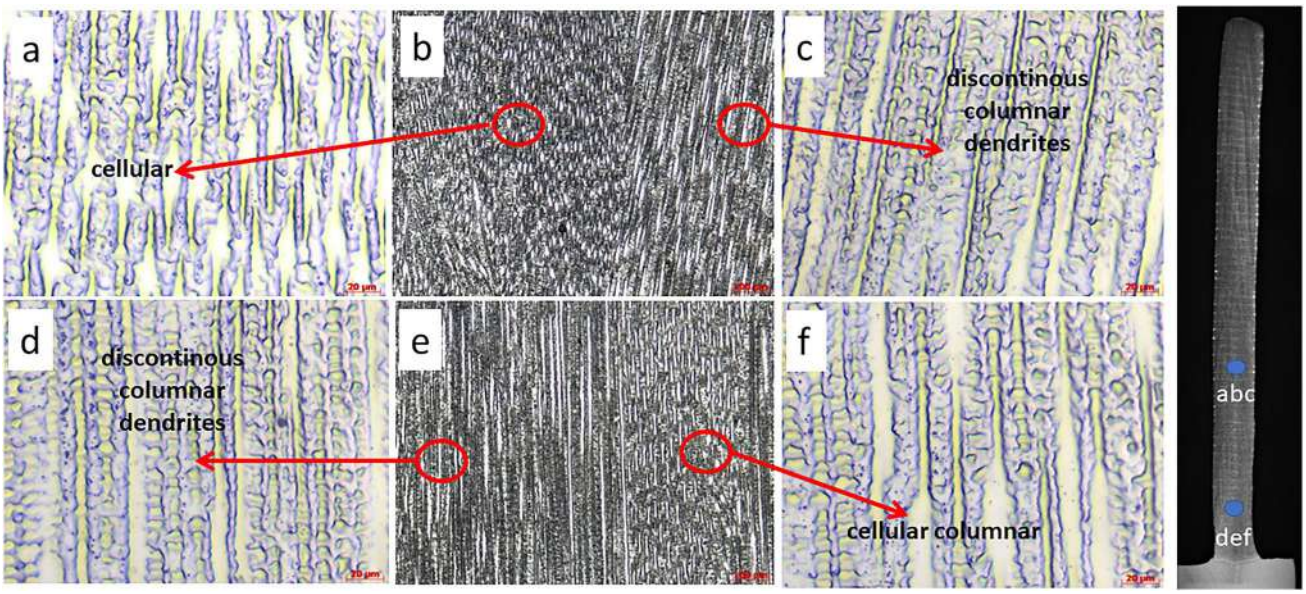

Fig. 3 Weld metal microstructure taken from bottom beads

type structure where A = Fe, Ni, Cr and B = Nb, Mo and Si. NbC is a secondary eutectic reaction [23] occurring at higher temperatures than Laves, both occurring in the final stage of the solidification. The distribution and size of the Laves phase in the deposited weld metal microstructure are determined by the form of the columnar or columnar/dendritic (continuous or discontinuous) structure that occurs following solidification. The secondary phases formed shapeless or eutectic morphology, remaining in between as for that the form of the grains during the solidification of the matrix, were bright phases along the dendrites. Laves phase is the final product of Ni-based filler metal such as ERNiCrMo-3, as it occurs in the final stage of solidification, and the solidification conditions can strongly influence the niobium decomposition and amount of Laves phase. During the solidification process, the precipitation of secondary phases, such as Laves and NbC, depletes many alloying elements, including niobium and molybdenum in the main matrix

[24]. An examination of the SEM image in Fig. 4a shows white-colored intermetallics appearing in the whole matrix and they were generated throughout the columnar structure direction. These intermetallics occurred between dendritic arms and had a disconnected layout from each other. The SEM image of segregation is given in Fig. 4b. According to the result of the elemental mapping taken from the relevant region, the elemental content of the intermetallics indicates the Laves phase rich in terms of Nb and Mo. The Laves phase, which is concentrated in the top part of the deposited weld metal, shows a partial decrease in the middle and root pass sequences.

SEM image and EDS analyses from the starting passes of deposited weld metal are given in Fig. 5. It is observed that Laves phases, which are detected more intensely in the top sequences, are less common in the bottom passes and are mixed with NbC phases seen like small dots. This effect is caused by the annealing of the top passes and is generated by the diffusion and dissolution of the elements. Laves phase melting occurs at a lower temperature and the melting point of NbC is higher than 3500 °C, which makes it difficult to melt during subsequent passes [21, 25]. The NbC formations, which appeared brighter than Laves phase, contained about 51% Nb and 21% C. In addition, it was determined that the Mo ratio of the columnar structure in the microstructure was higher than the matrix structure.

Yield strength (Rp0.2) and ultimate tensile stresses (UTS) of the deposited weld metal in all directions are shown in Table 2 and Fig. 6 graphically. The yield, strength, UTS and elongation were obtained by averaging three samples with standard deviation extracted from the same location. The tensile results revealed that the strength properties of the samples changed depending on the direction and showed a more ductile behavior in the angular direction. While the highest elongation was obtained in the samples extracted in angular direction with $55.5 \pm 2\%$, the lowest elongation was obtained from the samples from the transverse top region with 33.5 ± 1.5. Transverse specimens had the lowest elongation values. The tensile test results do not have a comparable correlation with the location that the samples were obtained. There was a clear effect of Laves and NbC phases on tensile strength. The annealing effect of the subsequent passes generated diffusion and dissolution of the elements [26]. Thus, the ratio of secondary phases decreased, and this effect caused an increase in fracture elongation. Moreover, it is important to point out that the ultimate tensile strength of the welding wire decreased in between 21 to 28% through each directions compared to certificate values shown in Table 2. Unlike the joining process, there was no base material dilution and the secondary phases were dissolved (decreased in the amount in the matrix) due to the high interpass temperature in the WAAM process. In addition to the high interpass temperature, the slow cooling rate also triggered the dissolution of intermetallic phases. Even though it produced an increase in elongation,

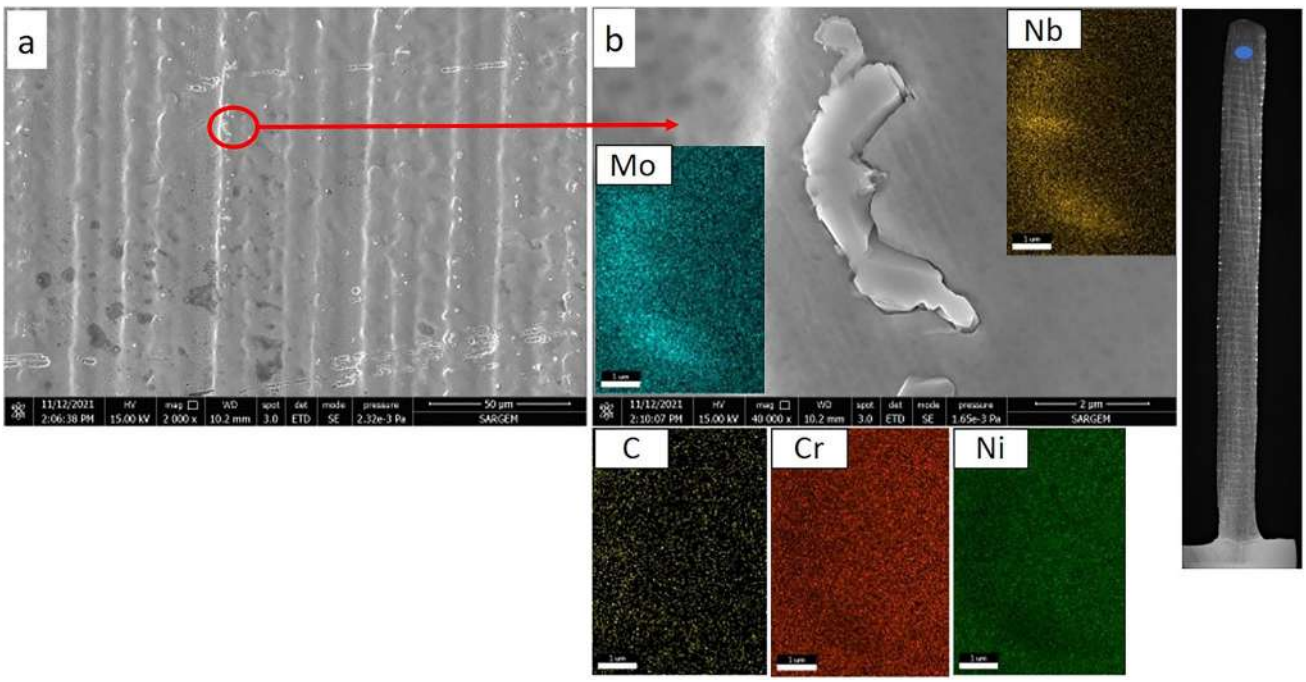

Fig. 4 SEM image of microstructure at face deposited weld metal and EDS mapping a) deposited weld metal microstructure b) intermetallic in deposited weld metal microstructure with high magnification and elemental mapping

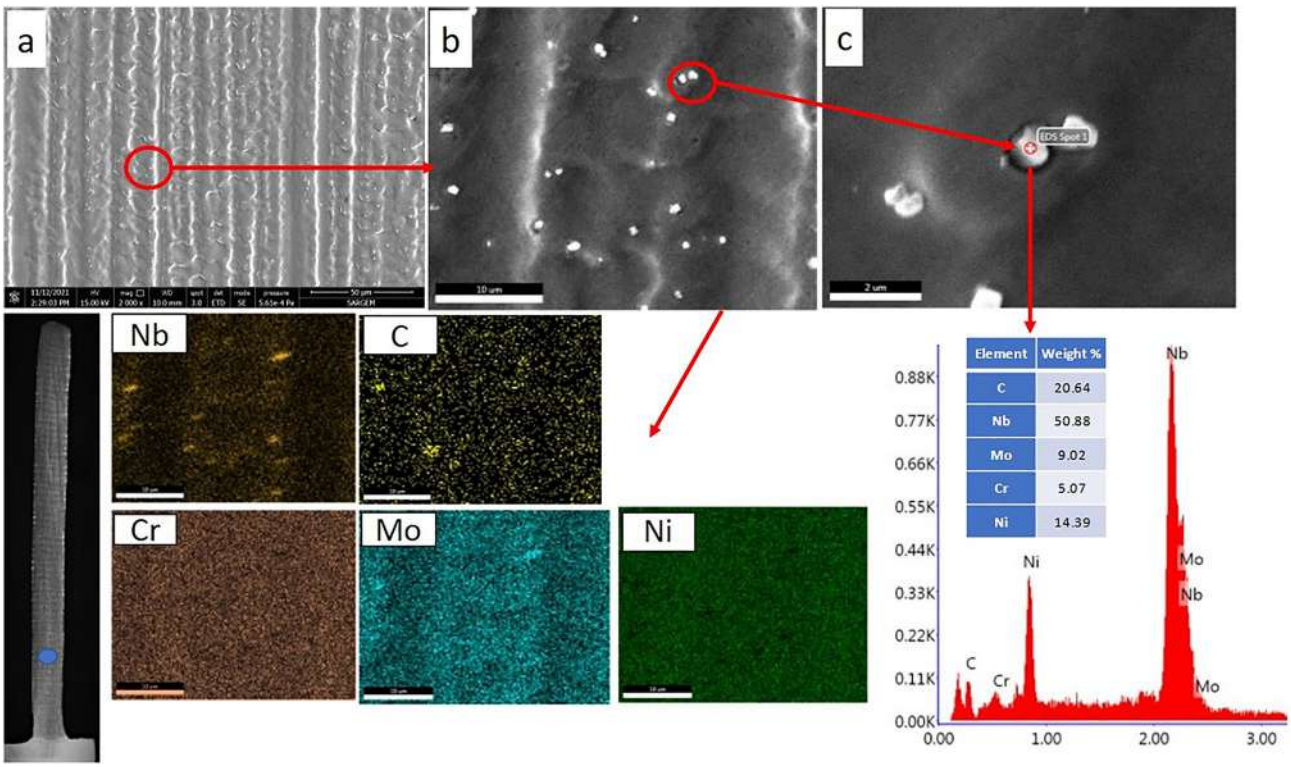

Fig. 5 SEM image of microstructure at bottom deposited weld metal and EDS mapping a) deposited weld metal microstructure b) intermetallic in deposited weld metal microstructure with high magnification and elemental mapping c) EDS analysis on NbC intermetallic

Table 2 Tensile test results based on extracted sample direction

Sample Direction	Rp0.2 (MPa)	Rm (MPa)	Fracture elongation (%)
Angular Top	438.5 ± 20.5	686.5 ± 32.5	48.5 ± 6.75
Angular Bottom	421.5 ± 15.5	698 ± 23	55.5 ± 2
Longitudinal Top	478.5 ± 21.5	627 ± 24	38.25 ± 3.25
Longitudinal Bottom	460 ± 24	641 ± 12	45 ± 5.75
Transverse Top	443 ± 51	638.5 ± 32.5	33.5 ± 1.5
Transverse Bottom	451 ± 9	641.5 ± 0.5	35 ± 6

it caused a decrease in the yield stress and UTS values due to the decrease in the limiting effect of deformation.

The stress–strain curves of the angular/longitudinal/transverse top and the angular/longitudinal/transverse bottom tensile samples are shown in Fig. 6a, b. The highest yield strength value was obtained from the longitudinal top sample with the 478.5 ± 21.5 MPa. The highest ultimate tensile stress value was obtained from the sample extracted from the angular bottom region with 698 ± 23 MPa. The lowest elongation was obtained from the samples extracted from the transverse top and bottom regions with 33.5 ± 1.5% and 35 ± 6% while the highest elongation was obtained in the samples extracted in angular top and bottom with 48.5 ± 6.75% and 55.5 ± 2%. The results confirmed the more pronounced difference with sample direction, indicating anisotropy in ductility. This effect, which is caused by the orientational difference during solidification in the microstructure, can improve the mechanical properties with the presence of fine grains.

Fracture surface SEM images taken from the bottom region after the tensile test are shown in Fig. 7 at low and high magnifications. All the fracture modes of the samples show ductile fracture. On fracture surfaces, dimples had very similar morphology in angular and longitudinal specimens, but dimples were wider in transverse specimens.

The hardness results were taken from the base material to the top point at 0.5 mm intervals, and the results are given in Fig. 8. The average hardness values measured at 10 mm ranges including standard deviation of the deposited weld metal are also given in Table 3. The results tend to be heterogeneous

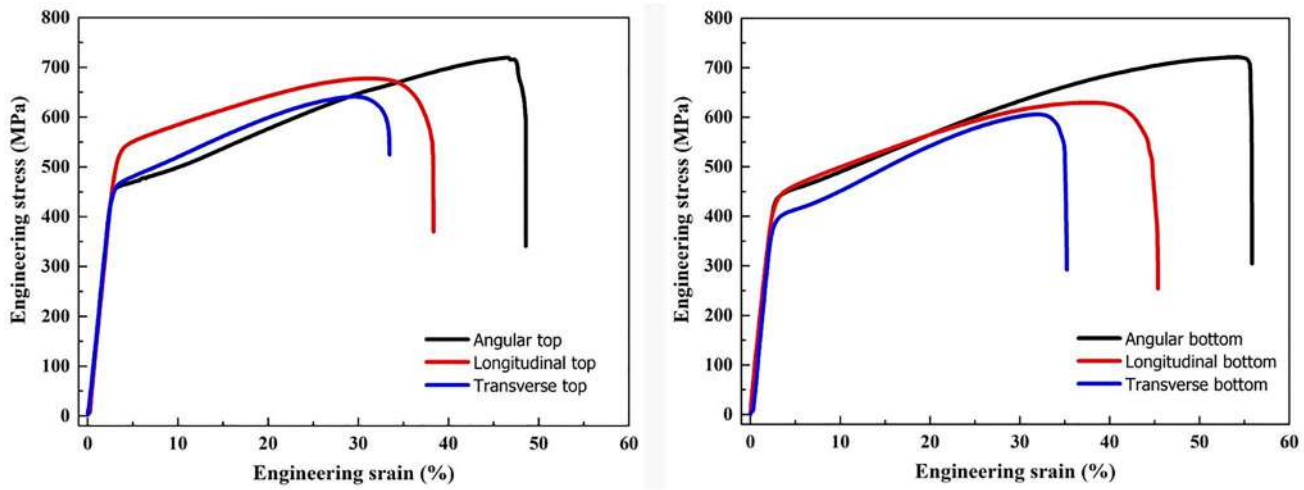

Fig. 6 Stress–strain curves of the angular/longitudinal/transverse top (a) and the angular/longitudinal/transverse bottom (b) samples

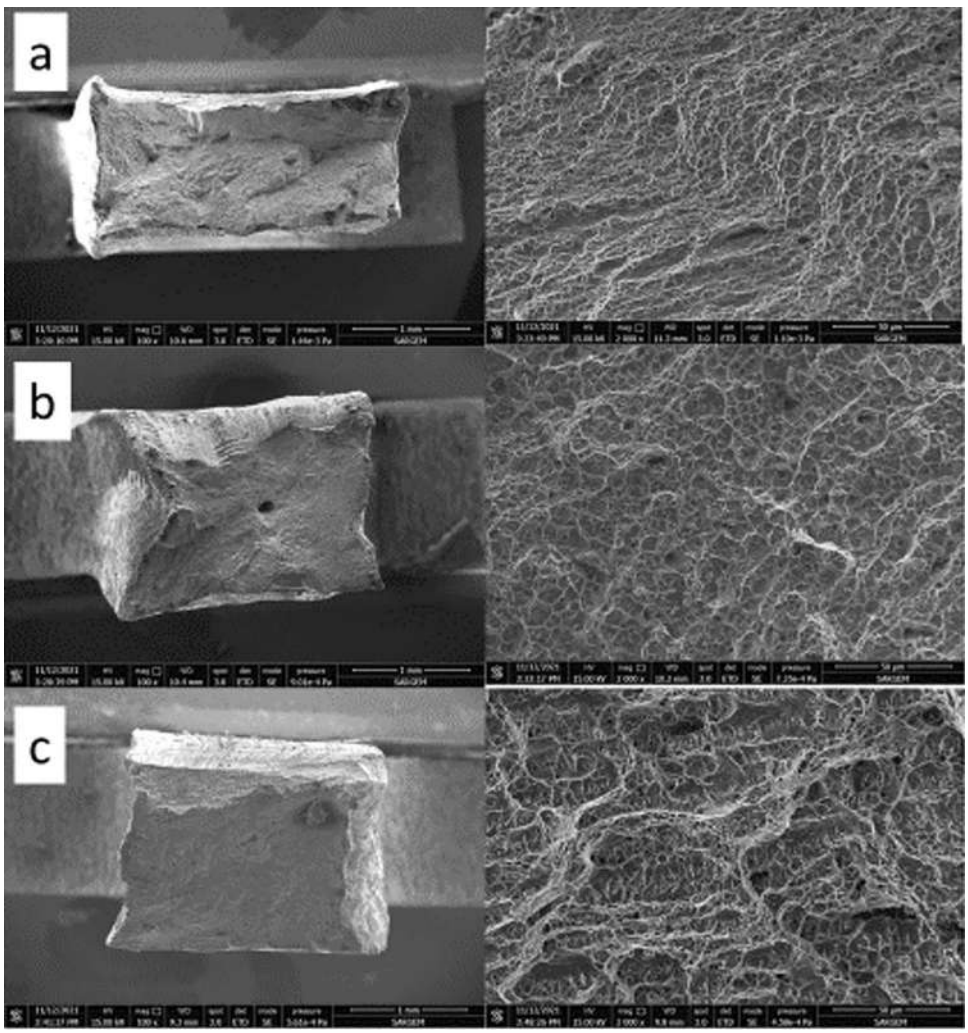

Fig. 7 Fracture surfaces after tensile tests (a) angular (b) longitudinal (c) transverse

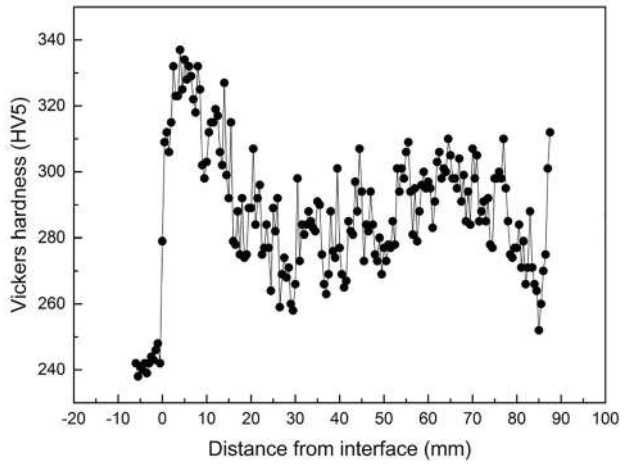

Fig. 8 Hardness distribution of the WAAM-produced component along the build direction

through to deposition direction, ranging from within different regions, ranging from 260 to 335 HV_5. The highest hardness value was reached about 318 ± 14 in the first up to 10 mm section. The different thermal conductivity between ERNiCrMo-3 deposited filler metal and the substrate metal caused rapid solidification. Furthermore, the hardness value at the interface increased due to greater dilution of Cr, Nb, Fe and Mo with the deposition of Inconel 625 on 304 L. This is the solid solution strengthening mechanism [3]. Similar results have been reported for welded joints and additive manufacturing of stainless steels and nickel-based superalloys [14, 27]. In the next section, the hardness value was more stable, and the average hardness did not exceed 300 HV_5 through next 80 mm. The general hardness value changed approximately between 275 ± 15 to 298 ± 16 HV_5 after 10 mm from the next. It cannot be said that the NbC and Laves phases have a significant effect on hardness. However, it is thought that the solidification mode affects the hardness due to the increase in the cooling rate in the bottom regions.

4 Conclusion

In the present work, defect-free Inconel 625 component was fabricated using the WAAM process using ERNiCrMo-3 filler wire. A novel geometry was built using robotic WAAM technology via Inconel 625 welding wire instead of building a simple wall geometry. A dense and close to final shape component was developed using robotic arc welding technology. The microstructural properties and mechanical responses were examined using test specimen. Additionally, micro-tensile test specimens which were extracted from the built through the three directions were systematically investigated. Furthermore, a continuous deposition pattern with increased and optimized travel speed was implemented via the robotic wire arc additive manufacturing process. All of the obtained results are given as follows:

(a) The microstructure of deposited weld metal consisted mainly of columnar dendrites. The morphology of the microstructure variation was in large dependent on the location of the deposited metal. In addition, the microstructure was composed of different solidification fronts and forms due to the thermal differences of the deposited weld metal.
(b) The deposited sample contained brittle Laves phases that were extremely low in root due to dissolution during tempering. However, the Nb content of the filler wire resulted in the formation of niobium carbides with irregular shapes. Moreover, the reduction of secondary phases in the weld metal microstructure due to repeated heat input caused an increased value of elongation.
(c) The lowest elongation values were obtained from the samples extracted from the transverse top and bottom regions with $33.5 \pm 1.5\%$ and $35 \pm 6\%$ while the highest elongation was obtained in angular top and bottom with $48.5 \pm 6.7\%$ and $55.5 \pm 2\%$, indicating anisotropy in ductility as direction-dependent.
(d) Obtaining microstructure and mechanical values depending on the direction due to unbalanced solidification are subjects to be considered in industrial applications. Furthermore, the free cooling conditions during welding and high interpass temperature reduce the intermetallic Laves phase ratio in the matrix microstructure. Thus, a remarkable decrease in strength and an increase in toughness of the welding wire have been provided.

Table 3 Measured hardness values depending on the distance from the substrate

Location (mm)	0–10	11–20	21–30	31–40	41–50	51–60	61–70	71–80	81–90
HV_5	318 ± 14	298 ± 16	278 ± 13	281 ± 11	281 ± 11	291 ± 11	297 ± 11	289 ± 10	275 ± 15

Acknowledgements Authors acknowledge the valuable contributions of Mr. Batuhan Turgut for assisting the robotic welding and the WAAM operations. Authors also thank Istanbul Gedik University Welding Technologies and Robot Technologies R&D Centers.

References

1. Frazier W E, *J Mater Eng Perform* **23** (2014) 1917. https://doi.org/10.1007/s11665-014-0958-z
2. Shankar V, Bhanu Sankara Rao K, and Mannan S L. *J Nucl Mater* **288** (2001) 222. https://doi.org/10.1016/S0022-3115(00)00723-6
3. Mohan Kumar S, Rajesh Kannan A, Pravin Kumar N, Pramod R, Siva Shanmugam N, Vishnu A S, et al., *J Mater Eng Perform* **30** (2021) 5692. https://doi.org/10.1007/s11665-021-05617-3
4. Ahsan M R U, Fan X, Seo G J, Ji C, Noakes M, Nycz A, et al., *J Mater Sci Technol* **74** (2021) 176. https://doi.org/10.1016/j.jmst.2020.10.001
5. Tanvir A N M, Ahsan M R U, Ji C, Hawkins W, Bates B, and Kim D B, *Int J Adv Manuf Technol* (2019) 3785. https://doi.org/10.1007/s00170-019-03828-6.
6. Tanvir A N M, Ahsan M R U, Seo G, Kim J duk, Ji C, Bates B, et al., *Int J Adv Manuf Technol* **110** (2020) 1709. https://doi.org/10.1007/s00170-020-05980-w.
7. Xu F, Lv Y, Liu Y, Shu F, He P, and Xu B, *J Mater Sci Technol* **29** (2013) 480. https://doi.org/10.1016/j.jmst.2013.02.010
8. Kumar K G, Ramkumar K D, and Arivazhagan N, *J Mech Sci Technol* **29** (2015) 1039. https://doi.org/10.1007/s12206-014-1112-4
9. Sridhar R, Devendranath Ramkumar K, and Arivazhagan N, *Acta Metall Sin (English Lett)* **27** (2014) 1018. https://doi.org/10.1007/s40195-014-0116-5
10. Ramkumar K D, Kumar P S G, Krishna V R, Chandrasekhar A, Dev S, Abraham W S, et al., *Mater Sci Eng A* **676** (2016) 88. https://doi.org/10.1016/j.msea.2016.08.104
11. Yangfan W, Xizhang C, and Chuanchu S, *Surf Coat Technol* **374** (2019) 116. https://doi.org/10.1016/j.surfcoat.2019.05.079
12. Altug-Peduk G S, Dilibal S, Harrysson O, and Ozbek S, *Russ J Non-Ferrous Met* **62** (2021) 357. https://doi.org/10.3103/S1067821221030020
13. Demiröz Ö B, and Dilibal S, *Int J 3D Print Technol Digit Ind* **5** (2021) 23. https://doi.org/10.46519/ij3dptdi.860678
14. Gürol U, Turgut B, Güleçyüz N, Dilibal S, and Koçak M, *Int J 3D Print Technol Digit Ind* **5** (2021) 721. https://doi.org/10.46519/ij3dptdi.1033374
15. Dinda G P, Dasgupta A K, and Mazumder J, *Mater Sci Eng A* **509** (2009) 98. https://doi.org/10.1016/j.msea.2009.01.009
16. Gonzalez J A, Mireles J, Stafford S W, Perez M A, Terrazas C A, and Wicker R B, *J Mater Process Technol* **264** (2019) 200. https://doi.org/10.1016/j.jmatprotec.2018.08.031
17. Gola K, Dubiel B, and Kalemba-Rec I, *J Mater Eng Perform* **29** (2020) 1528. https://doi.org/10.1007/s11665-020-04605-3
18. Zhang B, Bi G, Chew Y, Wang P, Ma G, Liu Y, et al., *Appl Surf Sci* **490** (2019) 522. https://doi.org/10.1016/j.apsusc.2019.06.008
19. Yin X, He G, Meng W, Xu Z, Hu L, and Ma Q, *J Mater Eng Perform* **29** (2020) 4222. https://doi.org/10.1007/s11665-020-04942-3
20. Nguejio J, Szmytka F, Hallais S, Tanguy A, Nardone S, and Godino Martinez M, *Mater Sci Eng A* **764** (2019) 138214. https://doi.org/10.1016/j.msea.2019.138214
21. DuPont N J, Lippold C J, and Kiser D S, (2009). https://doi.org/10.1017/CBO9781107415324.004.
22. Xing X, Di X, and Wang B, *J Alloys Compd* **593** (2014) 110. https://doi.org/10.1016/j.jallcom.2013.12.224
23. Naffakh H, Shamanian M, and Ashrafizadeh F, *Metall Mater Trans A Phys Metall Mater Sci* **39** (2008) 2403. https://doi.org/10.1007/s11661-008-9598-y
24. Xu F J, Lv Y H, Xu B S, Liu Y X, Shu F Y, and He P, *Mater Des* **45** (2013) 446. https://doi.org/10.1016/j.matdes.2012.07.013
25. Guo C, Ying M, Dang H, Hu R, and Chen F, *Mater Res Express* **8** (2021). https://doi.org/10.1088/2053-1591/abe977.
26. Tümer M, Mert T, and Karahan T, *Weld World* **65** (2020) 182. https://doi.org/10.1007/s40194-020-01011-0
27. Gürol U, *Int J Met* (2022). https://doi.org/10.1007/s40962-022-00834-5